Electrowetting-based enhancement of droplet growth dynamics and heat transfer during humid air condensation

Enakshi D. Wikramanayake, Vaibhav Bahadur *

Walker Department of Mechanical Engineering, The University of Texas at Austin, Austin, TX 78712, United States

ARTICLE INFO

ABSTRACT

Condensation heat transfer can be significantly enhanced by condensing vapor as droplets (instead of a film), which rapidly roll-off. This work studies the use of electrowetting to enhance coalescence, growth and roll-off dynamics of condensed droplets, thereby enhancing the condensation rate and associated heat transfer. This enhancement depends on the nature of fluid motion (translation of droplets, oscillations of the three phase line), which in turn depends on the magnitude and frequency of the applied electrical actuation waveform. Experiments are conducted to study early-stage droplet growth dynamics, as well as steady state condensation under the influence of an electric field. It is seen that droplet growth is enhanced as the voltage and frequency of AC electric fields is increased, with AC electric fields seen to be more effective than DC electric fields. Roll-off dynamics also depends on the frequency of the AC field. Overall, electric fields alter the droplet size distribution and move the condensate to more favorable states for removal from the surface. The condensation rate depends on the roll-off diameter of the droplet, frequency of roll-off events, and on the interactions of the rolled-off droplets with the remainder of the droplets. An analytical heat transfer model is utilized to relate the measured condensation rate with condensation heat transfer. It is noted that this study deals with condensation of humid air, and not pure steam. Overall, this study reports more than 30% enhancement in condensation rate resulting from the applied electric field, which highlights the attractiveness of electrowetting for condensation heat transfer enhancement.

© 2019 Elsevier Ltd. All rights reserved.

1. Introduction

Condensation of water is the basis of many applications including atmospheric water harvesting [1–3], power generation [4] and desalination [5,6]. The condensation rate and associated heat transfer is limited [7] by a condensate film on the surface; this occurs in most applications since metallic condenser surfaces are hydrophilic. Heat transfer is significantly enhanced if water condenses as drops which then roll-off [8], thereby exposing the surface to fresh vapor for re-nucleation. Dropwise condensation (DWC) [7] is observed on hydrophobic and superhydrophobic surfaces, which offer lower resistance to roll-off. Eliminating the thermal resistance of the film increases heat transfer coefficients by 5–10X [7] as compared to filmwise condensation.

DWC has been widely studied [7,9,10] from the objective of developing surfaces which enhance condensation heat transfer (CHT). There are three stages that a condensing fluid finds itself in during DWC [11,12]. Firstly, droplets nucleate and grow by direct vapor condensation on the surface. In the second stage, droplets grow rapidly by coalescence of neighboring droplets, which widens the droplet size distribution. In the third stage, sufficiently large droplets roll-off under gravity, and capture additional condensate droplets on their way down. Condensation dynamics and droplet size distributions have been studied on surfaces with a variety of textures and chemistry [9,13–16]. A majority of experimental studies on DWC have involved condensation of steam or saturated vapor; there exist fewer studies on condensation in the presence of non-condensable gases (NCGs), [14]. On the theoretical front, recent studies [8,17,18] have used measured droplet size distributions to estimate CHT using single droplet-based thermal resistance models.

In addition to surface engineering-based approaches, the use of an electric field to promote condensation heat transfer has generated significant recent interest [19–22]. Miljkovic et al. [23] used an electric field to prevent droplets jumping from the surface (due to the energy released via coalescence) from returning back; a 50% enhancement in heat transfer was measured. There also exist studies on the use of an electric field [24,25] to alter the surface

* Corresponding author.
E-mail address: vb@austin.utexas.edu (V. Bahadur).

tension of the condensing surface and condensed droplets, as a tool for enhancing DWC.

This work presents a study of the influence of electrowetting (EW) on condensation heat transfer enhancement. EW is a well-studied [26–29] fluid handling technique to control the wettability of droplets and enable microfluidic operations like the movement, splitting and merging of droplets. EW is based on the application of an electrical potential difference across a dielectric layer underlying the droplet (electrically conducting) to modulate wettability, and to actuate the droplet. The classical Young-Lippman's equation [26,30] predicts the voltage-dependent contact angle as:

$$\cos \theta = \cos \theta_{eq} + \frac{C}{2\gamma} V^2 \qquad (1)$$

where θ_{eq} is the equilibrium contact angle (no voltage), γ is the liquid-vapor interfacial tension, V is the applied voltage and C is the capacitance per unit area of the dielectric layer. The dielectric layer is a critical component of EW systems, with high dielectric constant, high electrical breakdown field and low surface energy being favorable attributes. Additionally, the dielectric material needs to be pin-hole free to prevent current flow.

The role of the frequency of the AC waveform used in EW actuation has been examined in prior studies. For context, a study of the influence of the AC frequency on condensation is a key aspect of the present work. For DC and low frequency AC waveforms, the droplet can be considered electrically conducting and equipotential (no electric field exists inside the liquid). However, at frequencies higher than the one corresponding to the charge relaxation time, the electric field begins to penetrate the droplet. The role of AC frequency is best understood by examining the expression for complex permittivity [26] of the droplet, $\varepsilon^* = k\varepsilon_0 - j\frac{\sigma}{\omega}$. Here k is the dielectric constant, σ is electrical conductivity and ω is the AC frequency. The first term represents the capacitance, and the second term represents the resistance. As the frequency increases, the relative influence of the electrical conductivity is reduced and the droplet behaves more as an insulator. In practice, low frequency AC fields are used in many EW applications, since contact angle hysteresis is lower for AC fields as compared to DC fields [26,28,30]. Under an AC field the contact line is continuously perturbed by the oscillating voltage; de-pinning becomes easier [26,30], which reduces hysteresis as compared to DC fields.

A significant number of studies on EW analyze EW-induced droplet motion, which is the key to the present study on EW-assisted droplet coalescence. The most commonly used configuration for EW-induced actuation of droplets consist of flat parallel plates separated by a fixed spacing. Arrays of individually addressable electrodes are fabricated on the bottom plate; the top plate acts as a common ground electrode to bias the droplet. The electrodes are covered with the EW dielectric layer and a hydrophobic topcoat to reduce the resistance to motion. When an electrode (on the bottom plate) adjacent to the droplet is turned on, electrostatic forces propel the droplet towards the center of the actuated electrode (which is the minimum energy position for that configuration). The actuation force that drives droplet motion depends on the change of the droplet area in contact with the actuated electrodes. For DC electric fields the EW force can be approximated as [27,28]:

$$F_{EW} = \frac{1}{2} V^2 \frac{dA}{dx} \left(\frac{k_d \varepsilon_0}{d} \right) \qquad (2)$$

where k_d is the dielectric constant of the dielectric layer, d is the thickness of the dielectric layer and $\frac{dA}{dx}$ is the change in area of the droplet in contact with the actuated electrode. The above equation estimates the force as the gradient of the electrostatic energy distribution. Also, droplet motion is opposed by contact line friction, viscous drag and wall shear forces [27]. In the present experiments,

the electrodes have a co-planar geometry where the positive and ground electrodes are in the same plane, separated by a non-conducting gap. In this case, the field lines form an arc from the high voltage electrode to the ground [24,31].

There exist five studies on the use of EW for condensation enhancement. The first study on EW and condensation was by Kim et al. [25], wherein an EW voltage was used to reduce the critical inclination angle for droplet roll-off. Experiments were first conducted using single droplets [25]; a later study involved removing condensate from evaporator fins [32]. In a more recent study, Baratian et al. [24] studied the coalescence of droplets condensing under the influence of a 1 kHz AC EW field. Energy-minimization considerations were used to explain condensation patterns and droplet size distributions. Another study from the same group showed that certain EW electrode configurations reduce droplet shedding radii and achieve faster roll-off, while other configurations trap droplets and hinder roll-off [33]. Yan et al. [34] showed that application of a DC electric field increased water shedding by inducing roll-off. However, this study involved condensation of mist droplets from a commercial water mister and cannot be directly compared with other studies on condensation which strictly involve condensation via phase change.

This manuscript details a fundamental study on EW-accelerated droplet growth dynamics and condensation heat transfer. Importantly, all experiments involve condensation of humid air (with significant non-condensables) unlike steam condensation which is the focus of a majority of existing studies. The influence of the applied voltage and frequency of the AC EW field on droplet growth and coalescence is experimentally characterized, and the underlying physical mechanisms are discussed. The influence of EW fields on condensation dynamics is studied both in the pre-droplet shedding phase, and in the droplet shedding phase. The CHT enhancement resulting from the EW fields is estimated by measuring the water condensation rate, which feeds into an analytical thermal resistance-based heat transfer model.

2. Experimental methods

2.1. Fabrication

The condensation experiments in this study were conducted in a single plate EW configuration with the high voltage and ground electrodes adjacent to each other. Indium Tin Oxide (ITO) coated glass slides were used as the substrate. Photolithography and plasma etching were used to pattern an interdigitated electrode layout (Fig. 1a). Details of the fabrication processes are included in the supplemental information. The two sets of electrodes were connected to the high voltage and ground ends of a signal generator and amplifier, to generate an electric field between adjacent electrodes. The electrode width and gap were 50 μm each. Fig. 1b shows the cross section of the condensation surface. A 2 μm layer of CYTOP (amorphous hydrophobic fluoropolymer) was spin coated on the surface as the EW dielectric. The dielectric layer is a critical requirement of EW systems, and stores electrostatic energy, which actuates the droplet. The condensing surface was placed (Fig. 1c) on a liquid nitrogen cold plate (Instec-mK1000 LN2-P), which maintained the surface at 2 ± 1 °C, to eliminate ice formation. The entire setup was placed in an environmental chamber (ESPEC Platinous H-series) maintained at 23 ± 2 °C and 60 ± 2.5% relative humidity. All experiments were conducted at atmospheric pressure.

2.2. Description of condensation experiments

Two types of experiments were presently conducted. The first type of experiments involved visualization of droplet growth
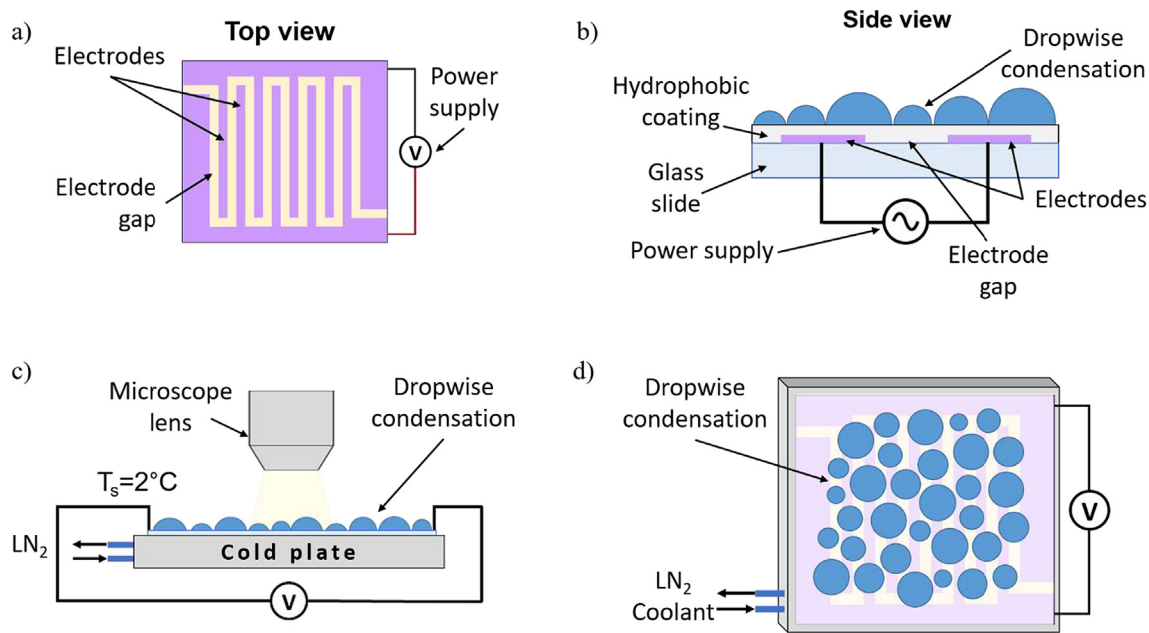
Fig. 1. Schematic of experimental setup. (a) Top view of condensation surface showing interdigitated electrode architecture. (b) Cross section of surface showing EW-related details. (c) Surface under optical microscope to visualize droplet growth dynamics. (d) Vertically oriented surface to study droplet roll-off.

dynamics on a horizontal surface (Fig. 1c). Condensation was prevented on the cold plate (by flowing a stream of nitrogen gas), while the temperature was ramped down. Once the plate reached a steady 2 °C, nitrogen flow was turned off, and the EW field was turned on. The electric field was kept on for the remainder of the experiments. Droplet growth was recorded with a 5X magnification lens of a Nikon Eclipse LV150N optical microscope. Experiments were conducted with 60 V rms (root mean square) and 100 V rms and at AC frequencies of 0 Hz (DC), 1 Hz and 10 kHz. Baseline experiments were conducted without any applied voltage. No experiments were conducted above 100 V to avoid breakdown of the dielectric layer. All experiments lasted 30 min and capture early-stage dynamics of droplet growth and coalescence.

For the second type of experiments, the surface was oriented vertically (Fig. 1d) and the experiments were conducted for longer durations. Droplets were seen to grow, coalesce and roll-off with the rolled-off droplets sweeping additional condensate as they left the surface. The amount of condensed water was estimated by cumulatively adding the mass of the droplets as they rolled to bottom of the condensing area, and was used to validate the heat transfer model detailed ahead. These experiments were conducted at 100 V rms and at AC frequencies of 1 Hz and 10 kHz. It is noted that all reported data in this study is the average of three repetitions.

Post-processing involved using MATLAB to count the number and size of condensed droplets (circle finder image processing script). The software and imaging capabilities allowed the detection of droplets larger than 5 μm. Droplets were assumed to have a spherical cap geometry, with a contact angle of 120° in the absence of an EW field. The EW voltage reduced the contact angle to as low as 90°. Measured voltage-dependent contact angles and a comparison with the predictions of the Young-Lippman's equation is included in the supplementary information.

3. Experimental results

3.1. Early stage droplet growth dynamics

This sub-section describes droplet growth dynamics under the influence of an EW field. Fig. 2 shows snapshots of the droplet size

distribution at 10 min and 30 min for the baseline (no voltage) case, 100 Vrms, 10 kHz case and 100 V DC case. A related video (video 1) is available in the supplemental material. At the beginning, droplets grow post-nucleation by condensation of vapor. Coalescence occurs once the droplets are large enough to contact adjacent droplets [11]. In the absence of an EW field (Fig. 2a and d), droplets maintain a self-similar and homogenous random pattern as the average droplet radius increases.

It is clearly seen that an electric field alters the droplet distribution. Droplets migrate to locations where the electrostatic energy of the system is minimized; the specific location depends on the electrode and droplet geometry and has been previously studied [26,27]. Droplets will migrate, when they are large enough (radii > 5–10 μm) for the electrostatic force to exceed the resistance due to contact angle hysteresis. Importantly, as the droplets grow, the electric field is itself modified (droplet is electrically conducting, compared to the insulating dielectric and air), and the minimum energy location can change [24].

Under AC fields, the minimum energy location is the center of the gap between adjacent electrodes [24,26,27]. Indeed, Fig. 2b shows droplets aligning along the electrode gaps (dark areas). As the droplets grow, they will merge, but they still prefer residing in the electrode gaps (Fig. 2e). Another notable observation is the role of the AC frequency on the type of droplet motion. At 10 kHz, droplets migrate to the minimum energy location, and remain there, with the triple phase line oscillating about the equilibrium position. However, at 1 Hz, droplets responds to the changing voltage by physically translating around their equilibrium positions (in addition to oscillations at the triple phase line). Both types of motions (oscillation, translation) will assist coalescence. Video 1 and Video 2 in the supplemental information demonstrate the two types of motion exhibited under high and low frequency electric fields. Contact-line motion is also favorable from the point of view of reducing pinning at the triple phase line. It is well-known that contact angle hysteresis and roll-off angles are lowered with AC electric fields [24,33].

For DC fields, the droplet arrangement has a different nature as compared to AC fields. When the droplets are large enough to be affected by the electric field, they first migrate to the interface between the ground electrode and the electrode gap (Fig. 3c). Sub-
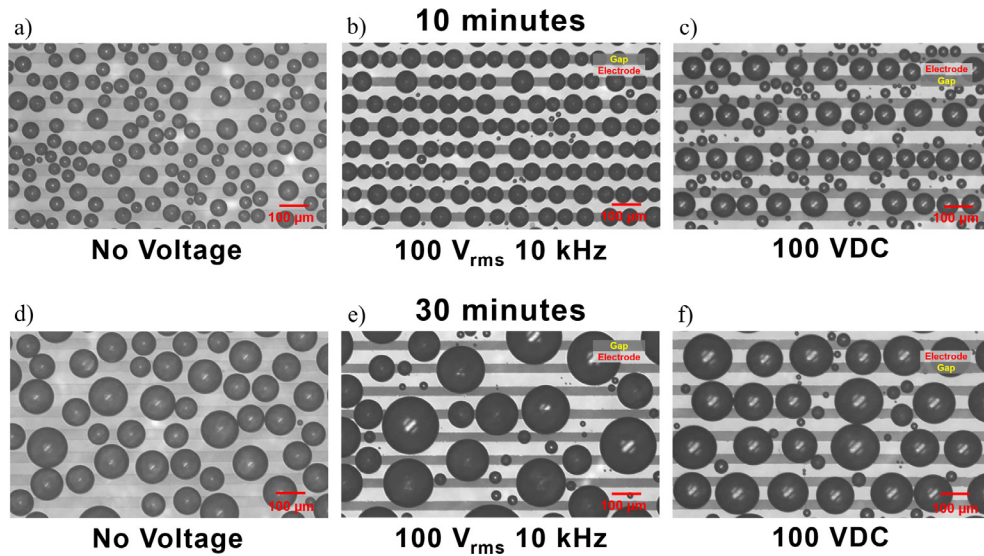
Fig. 2. Droplet growth patterns under (a) no voltage at 10 min, (b) 100 Vrms, 10 kHz at 10 min, (c) 100 VDC at 10 min, (d) no voltage at 30 min, (e) 100 Vrms, 10 kHz at 30 min, (f) 100 VDC at 30 min. The electrode width (light areas) and gap between electrodes (dark areas) is 50 μm.
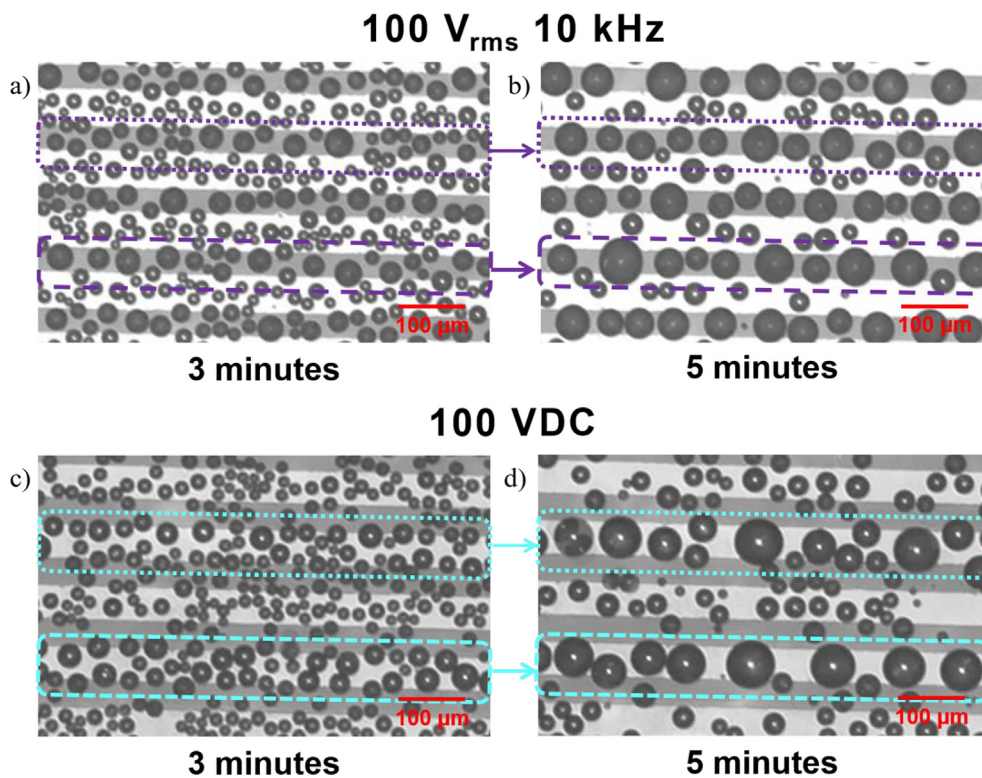

Fig. 3. Early stage droplet growth dynamics under AC and DC fields (a) 100 V rms, 10 kHz at 3 min, (b) 100 V rms, 10 kHz at 5 min (c) 100 V DC at 3 min, (d) 100 V DC at 5 min. The dotted lines show droplets aligning at 3 min and then merging to form larger droplets on the electrode gaps for the AC case (b), and alternate electrodes (d) for the DC case.

sequently, these droplets merge and then line up on the alternate electrodes. This is very clearly seen in Fig. 3d, which shows droplets lining along alternate electrodes. While this may seem non-intuitive, a previous energy minimization effort [27] clearly shows that droplets will line up on alternate electrodes if they are electrically grounded. The droplets remain here and continue to grow by condensation or coalescence as seen in Fig. 2c and f. Higher contact line friction (under DC electric fields) prevents them from moving unlike what is observed under AC fields. Fig. 3 highlights the differ-

ences in the coalescence patterns for the AC and DC cases, with droplets clearly lining up in the electrode gap for an AC field (Fig. 3a and b), and larger (coalesced) droplets lining up on alternate electrodes for the DC field (Fig. 3c and d).

The above discussions highlight the dependence of electric field-induced droplet growth dynamics on the nature of the electric field, electrode architecture and surface chemistry. Overall, triggering any type of droplet motion is beneficial for promoting coalescence and enhancing growth. To quantify the overall

influence of the electric field on growth dynamics, the area-weighted average droplet radius, $\langle R \rangle = \frac{\sum r^3}{\sum r^2}$ was estimated using the previously described image processing methodology. It is noted that during early stages of growth, the area-weighted average radius for baseline case is found to be equal to the average radius $\bar{R} = \frac{\sum_i r_i}{n}$, since the droplet size distribution has one dominant average radius.

Fig. 4 shows the evolution of $\langle R \rangle$ for applied voltages of 100 V rms (Fig. 4a) and 60 V rms (Fig. 4b), with frequencies of 1 Hz, 10 kHz and 0 Hz (DC voltage), along with the baseline case. It is clearly seen that an electric field accelerates growth dynamics, with the differences becoming more pronounced at longer times. At the end of 30 min $\langle R \rangle$ was higher than the baseline by 23% for 60 V (10 kHz) and 35% for 100 V (10 kHz). In general, faster droplet growth was observed for a 10 kHz waveform compared to a 1 Hz waveform. This suggests that the reduced contact angle hysteresis associated with high frequency AC fields [24,27] makes it easier for droplets to move and coalesce. Very interestingly, the DC electric field showed negligible improvement from the baseline case. For a DC field, the droplets migrate to the minimum energy position and remain there. The absence of oscillatory motion of the contact line reduces the possibility of larger droplets capturing smaller ones. Droplets can only grow by further vapor condensation or via translation of newer droplets, which is also challenging due to the larger hysteresis associated with DC fields. The nature of

the electric field lines will also be different for AC versus DC fields. For DC fields, the droplet is considered equipotential, however AC fields will penetrate inside the droplet (this effect becomes more significant with an increase in frequency).

The influence of electric fields can also be quantified by analyzing the rate of droplet growth (rate of change of area-averaged radius) $\frac{d\langle R \rangle}{dt}$. For the baseline case (Fig. 5), the growth rate of the average radius decreased and plateaued to a constant value, as also reported by Leach et al. [12]. Under AC fields, $\frac{d\langle R \rangle}{dt}$ shows a decaying oscillatory trend with time. The increase in droplet growth rate, or positive slope regions of this curve are due to electric field-based coalescence cascades. After one cascade droplets settle in their new equilibrium locations, and additional coalescence is prevented for some time, since they are too small to contact the neighboring droplet. Accordingly, the growth rate slows down (negative slope region), with condensation being the growth driver. When these droplets (fed by new condensate) become large enough to 'see' the neighboring droplets, an electric-field based coalescence cascade occurs again (positive slope region). For a DC field, there is an initial increase in growth rate when the influence of an electric field is first seen. However, droplets do not oscillate, and subsequent growth rate reduces as direct vapor condensation becomes the dominant mechanism, along with the translation of newly nucleated droplets.

The impact of electric fields on droplet size distributions after 30 min is depicted in Fig. 6. For the baseline case, a unimodal
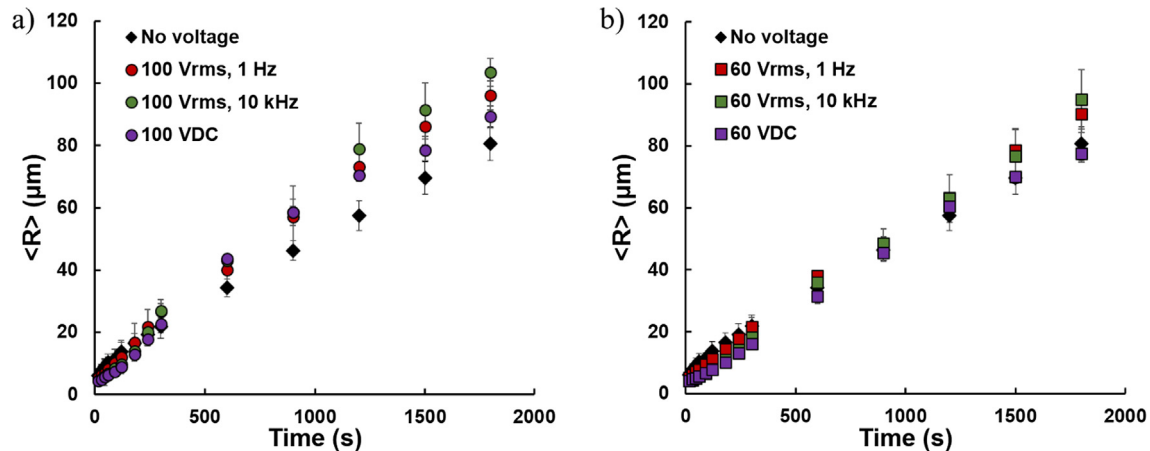

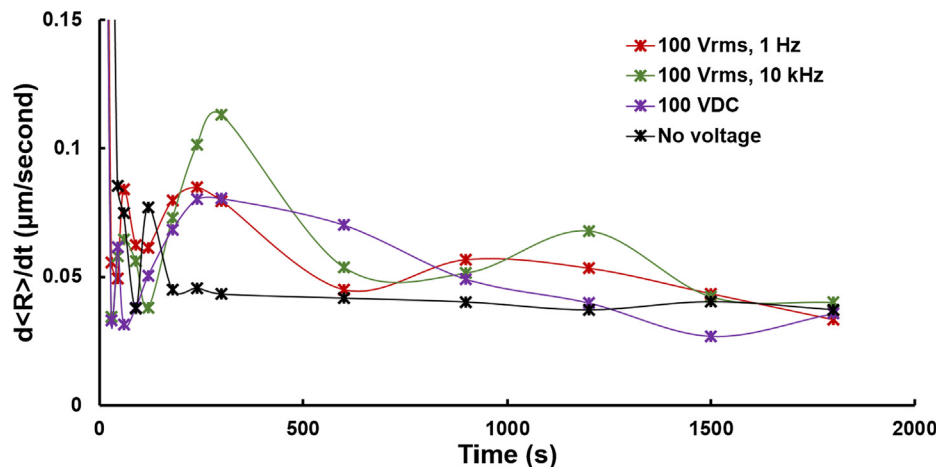**Fig. 4.** Area-weighted average radius of condensed droplets versus time under EW voltages of (a) 100 V and (b) 60 V.

Fig. 5. Rate of change of area-averaged droplet radius for 100 Vrms AC fields, 100 VDC field and baseline cases.
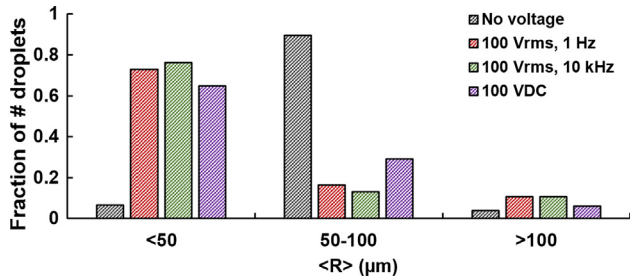
Fig. 6. Distribution of sizes of droplets condensing under the influence of electric fields after 30 min.

log-normal distribution is observed which shows a decreasing average radius and a widening droplet size distribution over time until roll-off. Under an electric field, a bi-modal or multi-modal distribution [24] is observed, wherein large droplets are surrounded by many small droplets. Although the distribution shows a smaller number density in the larger size bin, the larger droplets account for a significantly greater volume (volume scales as r^3) percentage of the condensate. At 30 min, the total condensate volume in the largest bin (>100 μm) for 100 V rms AC is 3X greater than in the no voltage case. This again highlights the influence of an electric field in moving condensate to a state favorable for removal.

Knowledge of droplet size distributions is used to estimate the heat transfer rate, as detailed ahead. Droplet size distribution is also critical to overall enhancement of CHT. While smaller droplets enhance heat transfer locally (lower thermal resistance), larger droplets sweep away significant condensate when they detach, thereby exposing fresh surfaces for nucleation (this is seen in video 3 and 4 in the supplemental information). Additionally, increased condensation rates will lead to more frequent sweeping events. All these considerations are suggestive of an optimum distribution that maximizes heat transfer; this can be explored in a future study.

3.2. Droplet roll-off and condensation rate under the influence of electric fields

This section discusses experiments with vertically oriented surfaces, which allowed the droplets to roll-off. These experiments were run for 3 hours. The condensation rate was obtained by cumulatively adding the mass of droplets rolled-off over time.

Droplet mass was estimated using image analysis to find the radius (hence volume) of the spherical cap shaped droplet after it had rolled off the active condensation area. Fig. 7a shows the condensation mass flux (average of three experiments) for various cases. Droplet roll-off occurs when the coalesced droplets have reached a critical radius. Thereafter, the condensed mass flux is estimated using the procedure outlined above. For the cases of no voltage and 100 V, 10 kHz, two regions of the curve (Fig. 7a) can be identified. The initial, higher slope region accounts for a large number of roll-off events taking place between the times corresponding to roll-off of the first droplet, till the time that the entire area is swept at least once. The second region corresponds to a lower and constant slope (constant condensation rate), which is maintained for the remainder of the experiment. This regime is referred to as steady state wherein droplet nucleation, growth, coalescence, and roll-off occur at various places on the surface [12,35]. This is a quasi-steady process with a stable droplet size distribution and a steady rate of heat transfer. Under these conditions, classical models can be used to characterize the number density of droplets [36].

Presently, the first roll-off event for the baseline case occurred at ~60 min. The average roll-off radius was 725 ± 89 μm. In this case, droplets maintain a random self-similar pattern (regardless of the size), which results in a stable droplet size distribution. For the case of 100 V, 1 Hz, the first roll-off event occurred at ~30 min, and average roll-off radius was 420 ± 100 μm. The reason for the lower roll-off radius is the reduction in contact angle hysteresis associated with AC electric fields. Droplets are observed to oscillate around their mean positions as seen in video 2. The two parts of video 2 show oscillatory motion of large droplets before they have rolled-off, and translation motion of smaller droplets which have nucleated in the track exposed by a droplet that rolled-off. For the 100 V, 10 kHz case, the first roll-off event occurred at ~70 min with an average roll-off radius of 730 ± 75 μm. This delayed roll-off can be attributed to the electric field pinning droplets to the surface [33], noting that the electric field lines will penetrate the droplet at such frequencies. This suggests that periodically turning the electric field off could assist in droplet roll-off for such cases. It is also noted that larger droplet roll-off radii are not necessarily detrimental to overall condensation, since the droplet size determines the amount of condensate swept in the path of the droplet. It is also noted that the electrodes were oriented vertically, which significantly reduces the electrostatic resistance to droplet roll-off along the equipotential electrode surface.
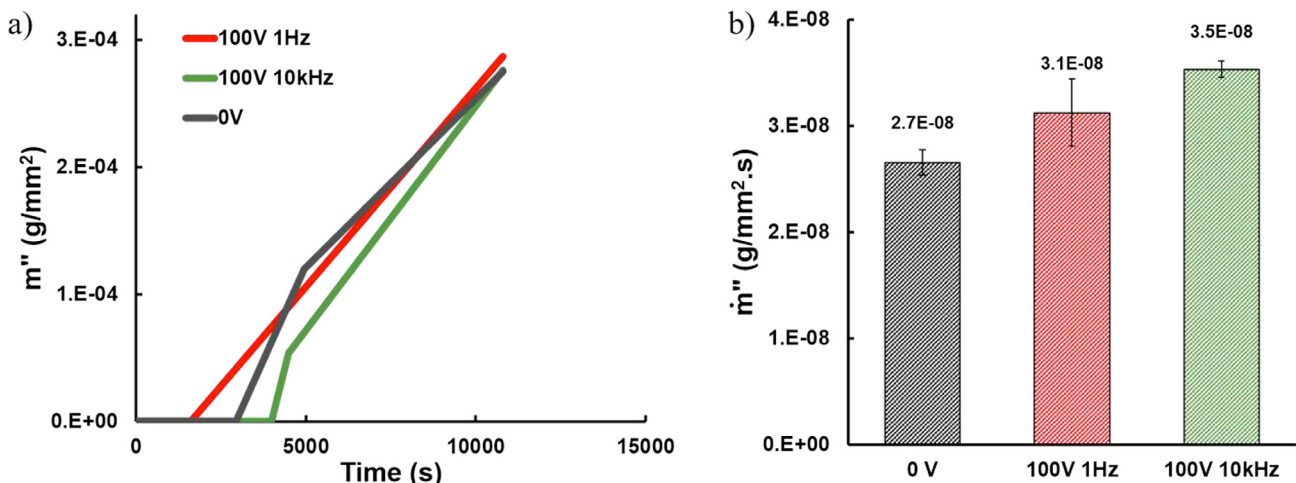

Fig. 7. (a) Condensed mass flux versus time for three cases (no voltage, 100 V, 10 kHz, and 100 V, 1 Hz), and (b) Steady state condensation rate for the three cases.

Fig. 7b shows the steady state condensation rates for the three cases (raw data for these measurements is available in the supplemental information). The 100 V, 10 kHz case has the highest condensation rate, which is 33% higher than the baseline case. This corresponds to largest droplet roll-off radius and the lowest frequency at which droplets roll-off. The large droplets capture a significant number of smaller droplets on their way down, thereby opening up a large new track for fresh nucleation. For the 100 V, 1 Hz case, the condensation rate is 17% higher than the baseline case. This case is characterized by a relatively low roll-off radius and high frequency of roll-off events. Since the roll-off frequency is high, there is lesser time for droplets to grow. Consequently, smaller droplets are swept away as compared to the 100 V, 10 kHz case. These numbers suggest that overall condensation need not be maximized by droplets rolling-off rapidly and at smaller sizes, but also involves consideration of the interactions of the rolling-off droplets with the rest of the distribution.

4. Heat transfer modeling

This section details first-order models to relate the measured water collection to CHT. A thermal resistance network-based analytical model is first described, which predicts CHT for a specified droplet size distribution. This model is used to predict the heat transfer for the baseline case. Interestingly, it is seen that the predictions from this model reasonably match the predictions of another thermodynamics-based first-order model, which requires the water collection rate as the input (instead of droplet size distribution). This thermodynamics-based model is therefore used to predict CHT under EW fields. It is noted these models constitute the first detailed assessment of the benefits of EW on CHT enhancement.

The thermal resistance network-based heat transfer model is briefly described ahead, and extends the recent work of Zhoa et al. [13] Historically, similar models have been used for CHT analysis; however all the studies involved DWC under saturated vapor conditions [8,17,18]. In the present experiments with humid air, the thermal resistance network is modified to account for the presence of non-condensable gases. It is well-known that the presence of non-condensables drastically reduces CHT [13,15]. The thermal resistance network in this work also considers natural convection from the non-wetted area, which is an improvement over existing models which only consider heat transfer through the condensed droplets.
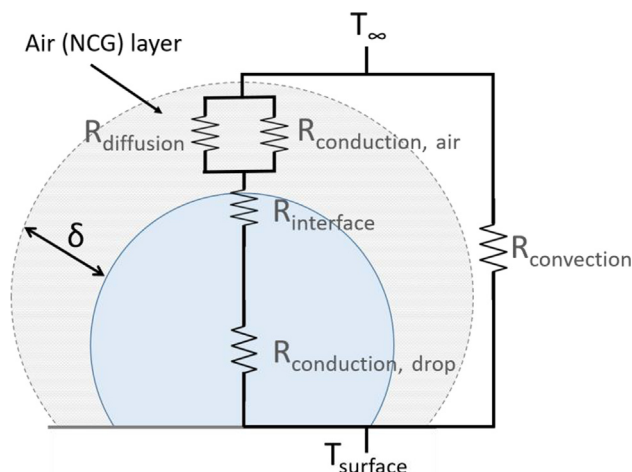

Fig. 8. Thermal resistance network corresponding to a single droplet in dropwise condensation mode.

Fig. 8 shows the thermal resistance network (corresponding to a single droplet) for DWC in the presence of non-condensables. As water vapor condenses, a layer of non-condensables accumulates at the liquid-vapor interface around the droplet. The water vapor in ambient air diffuses through this boundary layer to reach the droplet, which imposes a conduction resistance through air. This boundary layer offers the largest thermal resistance in the heat transfer network [15,37]. Zhoa et al. [13] modeled this boundary layer as containing two resistances in parallel which transfer heat from the ambient air at T_∞ to the surface of the droplet at T_i; a similar approach is presently used. The resistance associated with diffusion of vapor through the layer of non-condensables [13] is:

$$R_{diff} = \frac{(T_\infty - T_i)}{\dot{m}h_{fg}} \qquad (3)$$

where $\dot{m}$ is the condensation rate based on experimental data, h_{fg} is the latent heat of condensation, and T_i and T_∞ are the interface and ambient temperatures, respectively. The conduction resistance of air [13] is estimated as:

$$R_{cond,air} = \frac{\delta}{k_{air}S(r)} \qquad (4)$$

where k_{air} is the thermal conductivity of air and $S(r)$ is the projected area of the droplet. In Eq. (4), δ is the thickness of the boundary layer, which in an unknown. However, by equating the condensation rate to the mass diffusion rate [13,38], an approximation for δ can be obtained using:

$$\dot{m}'' = -\mathcal{D}Mc\frac{x_i - x_\infty}{\delta} \qquad (5)$$

where $\mathcal{D}$ is the diffusion coefficient of water vapor in air, c is the concentration and M is the molecular weight of water. x_∞ is the mole fraction in water, determined by ambient conditions $\left(x_\infty = RH\frac{P_{sat}}{P_\infty}\right)$, where P_{sat} is the saturation pressure and P_∞ is the ambient (atmospheric) pressure. x_i is the mole fraction at the liquid-vapor interface of the droplet determined by the Clausius-Clapeyron equation [39] as:

$$x_i = \exp\left[-\frac{h_{fg}}{R}\left(\frac{1}{T_i} - \frac{1}{T_{boil}}\right)\right] \qquad (6)$$

where T_{boil} is the boiling point under atmospheric pressure (P_∞).

Next, the thermal resistance associated with the droplet is considered, based on existing classical droplet thermal resistance models [7,8,39]. This network consists of an interface resistance and conduction resistance in series [7,8,17,18]. The interface resistance [18,39] accounts for the temperature drop at the vapor-liquid interface, and is estimated as:

$$R_{int} = \frac{1}{h_i 2\pi r^2(1 - cos\theta)} \qquad (7)$$

h_i is the interfacial heat transfer coefficient [8,39] expressed as:

$$h_i = \frac{2\alpha}{2 - \alpha}\frac{1}{\sqrt{2\pi R_g T_s}}\frac{h_{fg}^2}{v_g T_s} \qquad (8)$$

where θ is the contact angle and R_g is the specific gas constant. The accommodation coefficient (condensation coefficient), α is the fraction of vapor molecules that move into the liquid droplet during phase change and is found to be in the range of 0.02–0.04 for water [39]. In this work, we use $\alpha = 0.02$ to represent the low humidity conditions of present experiments. Finally, the conduction resistance of the droplets is expressed as [18]:

$$R_{cond,drop} = \frac{\theta}{4\pi k_l r sin\theta} \qquad (9)$$

where k_l is the thermal conductivity of water. The overall thermal resistance can be estimated as:

$$R_{Total}(r) = \left[\frac{1}{R_{diff}} + \frac{1}{R_{cond,air}}\right]^{-1} + R_{int} + R_{cond,drop} \tag{10}$$

The droplet radius dependent heat transfer can then be expressed as:

$$q(r) = \frac{\Delta T}{R_{Total}(r)} \tag{11}$$

where $\Delta T = T_\infty - T_{surface}$. From a knowledge of droplet size distribution and consideration of natural convection, the overall surface heat flux can be estimated as [8]:

$$q''_{surface} = \int_{R_{min}}^{R_{max}} q(r)N(r)dr + f_{dry} * h_{air} * (T_\infty - T_s) \tag{12}$$

In the above equation, the first term on the right is the heat flow through all the droplets. $N(r)$ is the number density of droplets at a given time instant. The second term on the right accounts for natural convection through the non-wetted area around the droplet, where f_{dry} is the fraction of dry area and h_{air} is the heat transfer coefficient (method used to estimate h_{air} is described in the supplemental information). This model predicts a steady-state CHT of 104 W/m^2 for the baseline case, based on the droplet size distribution. While this is a low value of flux compared to most studies on condensation, it is noted that this work involves condensation of humid air and not pure steam (unlike most studies); furthermore, there are no forced convection effects here. It is also seen that the effective thermal resistance of the network is well-approximated by the conduction resistance through air, with the droplet resistance being negligible; this is to be expected due to the presence of non-condensables. A comparison of various thermal resistances is included in the supplementary information.

Another estimate for the heat flux estimate can be arrived at by a first-order thermodynamics-based assessment. From the knowledge of the measured condensation rate $\dot{m}''$ and the wetted fraction, the overall heat transfer can be estimated as:

$$Q'' = \dot{m}''h_{fg} + \dot{m}''C_{p,wv}(T_\infty - T_{dp}) + f_{dry} * h_{air}(T_\infty - T_s) \tag{13}$$

It is noted that a similar approach was used to predict CHT associated with atmospheric water harvesting applications [40]. The first term on the right side in Eq. (13) accounts for latent heat of condensation h_{fg} (2270 kJ/kg). The second term accounts for sensible cooling of vapor (which eventually condenses) and the third term accounts for natural convection-based heat gain by the dry surface area (detailed in supplementary information). $C_{p,wv}$ is the specific heat of vapor, and T_∞ and T_{dp} are the ambient and dew point temperatures respectively. Comparison of these terms shows that the contribution of sensible cooling is negligible. For the baseline case, latent heat and natural convection represent 71% and 29% of the total flux, respectively. The relative contribution of the latent heat term increases with an increase in the condensation rate. For the 100 V, 10 kHz case where the mass flux is highest, latent heat and natural convection shows the same breakdown of the total flux as the baseline case.

This thermodynamics-based model (Eq. (13)) predicts a condensation heat flux of 85 W/m^2 for the no voltage case. This is a reasonable match with the prediction of the thermal resistance network-based model (104 W/m^2), considering the simplicity and the significant assumptions involved in the formulation. The thermodynamics-based model requires knowledge of the condensation rate and the surface wetted fraction (which is often reported in literature [11,12,24]), and does not require knowledge of droplet size distributions, which can be challenging to obtain. Using this

model for the cases of condensation under EW fields results in heat transfer rates of 102 W/m^2 and 111 W/m^2 for the 100 V, 1 Hz and 100 V, 10 kHz cases, respectively. When compared to the baseline case, there is a 21% and 31% enhancement for the 100 V, 1 Hz and 100 V, 10 kHz cases, respectively. Note that the enhancement in the condensation rate is different from the enhancement in condensation heat flux. This difference is due to the natural convection term in condensation heat transfer, which makes the relationship between CHT and condensation rate non-linear.

5. Conclusions

Overall, this study shows that electric fields can significantly influence coalescence and growth dynamics during condensation of humid air. Controlling factors include the magnitude and frequency of the applied waveform and the electrode architecture. It is seen that AC fields promote greater coalescence than DC fields, with higher frequencies increasing droplet growth rate. The roll-off dynamics is also altered by the electric fields, and it is possible to control the roll-off size and frequency by controlling the applied waveform. Total condensate removal depends on the size and frequency of droplets rolling off, and also on the amount of liquid captured by the droplet as it departs. Condensate removal enhances heat transfer; heat transfer enhancements of up to 31% was observed in this study. This study suggests several avenues for further CHT enhancement. Numerous additional strategies can be employed to enhance droplet coalescence, such as the use of waveforms of various shapes, periodic use of an electric field and the use of a traveling electric field etc. Such strategies, along with the nature of the field, and the surface chemistry (which governs contact angle and hysteresis) will influence the growth, coalescence, and roll-off kinetics, which determines heat transfer.

Declaration of Competing Interest

The authors declare no conflict of interest.

Acknowledgements

Appendix A. Supplementary material

Supplementary data to this article can be found online at https://doi.org/10.1016/j.ijheatmasstransfer.2019.05.112.

References

[1] O. Ozkan, E.D. Wikramanayake, V. Bahadur, Modeling humid air condensation in waste natural gas-powered atmospheric water harvesting systems, Appl. Therm. Eng. 118 (2017) 224–232.

[2] K.-C. Park, S.S. Chhatre, S. Srinivasan, R.E. Cohen, G.H. McKinley, Optimal design of permeable fiber network structures for fog harvesting, Langmuir 29 (2013) 13269–13277.

[3] H. Kim et al., Water harvesting from air with metal-organic frameworks powered by natural sunlight, Science 356 (2017) 430–434.

[4] A.T. Paxson, J.L. Yagüe, K.K. Gleason, K.K. Varanasi, Stable dropwise condensation for enhancing heat transfer via the Initiated Chemical Vapor Deposition (iCVD) of grafted polymer films, Adv. Mater. 26 (2014) 418–423.

[5] V.G. Reifert, A.I. Sardak, S.V. Grigorenko, V.L. Podbereznyj, Heat exchange at dropwise condensation in heat exchangers of desalination plants, Desalination 74 (1989) 373–382.

[6] S. Parekh, M.M. Farid, J.R. Selman, S. Al-hallaj, Solar desalination with a humidification-dehumidification technique — a comprehensive technical review, Desalination 160 (2004) 167–186.

[7] J.W. Rose, Dropwise condensation theory and experiment: A review, Proc. Inst. Mech. Eng. Part A J. Power Energy 216 (2002) 115–128.

[8] N. Miljkovic, R. Enright, E.N. Wang, Modeling and optimization of superhydrophobic condensation, J. Heat Transf. 135 (2013) 111004.

[9] A. Azar, V. Bahadur, A. Kulkarni, M. Yamada, J.A. Ruud, Hydrophobic surfaces for control and enhancement of water phase transitions, MRS Bull. Interfacial Mater. Spec. Wettability 38 (2013) 407–411.

[10] N. Miljkovic, R. Enright, E.N. Wang, Effect of droplet morphology on growth dynamics and heat transfer during condensation on superhydrophobic nanostructured surfaces, ACS Nano 6 (2012) 1776–1785.

[11] J.E. Castillo, J.A. Weibel, S.V. Garimella, The effect of relative humidity on dropwise condensation dynamics, Int. J. Heat Mass Transf. 80 (2015) 759–766.

[12] R.N. Leach, F. Stevens, S.C. Langford, J.T. Dickinson, Dropwise condensation: experiments and simulations of nucleation and growth of water drops in a cooling system, Langmuir 22 (2006) 8864–8872.

[13] Y. Zhao et al., Effects of millimetric geometric features on dropwise condensation under different vapor conditions, Int. J. Heat Mass Transf. 119 (2018) 931–938.

[14] P.B. Weisensee et al., Condensate droplet size distribution on lubricant-infused surfaces, Int. J. Heat Mass Transf. 109 (2017) 187–199.

[15] B. Mondal et al., Design and fabrication of a hybrid superhydrophobic-hydrophilic surface that exhibits stable dropwise condensation, ACS Appl. Mater. Interfaces 7 (2015) 23575–23588.

[16] F. Chu, X. Wu, Q. Ma, Condensed droplet growth on surfaces with various wettability, Appl. Therm. Eng. 115 (2017) 1101–1108.

[17] N. Miljkovic, R. Enright, E.N. Wang, Growth dynamics during dropwise condensation on nanostructured superhydrophobic surfaces, ASME 2012 3rd Micro/Nanoscale Heat & Mass Transfer International Conference MNHMT2012, vol. 1, 2012, pp. 1–10.

[18] S. Kim, K.J. Kim, Dropwise condensation modeling suitable for superhydrophobic surfaces, J. Heat Transf. 133 (2011) 081502.

[19] P. Birbarah, Z. Li, A. Pauls, N. Miljkovic, A comprehensive model of electric-field-enhanced jumping-droplet condensation on superhydrophobic surfaces, Langmuir 31 (2015) 7885–7896.

[20] X. Yan et al., Droplet condensation on superhydrophobic surfaces with enhanced dewetting under a tangential AC electric field, Appl. Phys. Lett. 109 (2016).

[21] T. Foulkes et al., Active hot spot cooling of GaN transistors with electric field enhanced jumping droplet condensation, in: Conf. Proc. - IEEE Appl. Power Electron. Conf. Expo. - APEC, 2017, pp. 912–918, https://doi.org/10.1109/APEC.2017.7930805.

[22] A. Shahriari, P. Birbarah, J. Oh, N. Miljkovic, V. Bahadur, Electric field-based control and enhancement of boiling and condensation, Nanoscale Microscale Thermophys. Eng. 21 (2017) 102–121.

[23] N. Miljkovic, D.J. Preston, R. Enright, E.N. Wang, Electric-field-enhanced condensation on superhydrophobic nanostructured surfaces, ACS Nano 7 (2013) 11043–11054.

[24] D. Baratian, R. Dey, H. Hoek, D. Van Den Ende, F. Mugele, Breath figures under electrowetting: electrically controlled evolution of drop condensation patterns, Phys. Rev. Lett. 120 (2018) 214502.

[25] J. Kim, M. Kaviany, Purging of dropwise condensate by electrowetting, J. Appl. Phys. 101 (2007).

[26] F. Mugele, J.-C. Baret, Electrowetting: from basics to applications, J. Phys. Condens. Matter 17 (2005) R705–R774.

[27] V. Bahadur, S.V. Garimella, An energy-based model for electrowetting-induced droplet actuation, J. Micromech. Microeng. 6 (2006) 1494–1503.

[28] N. Kumari, V. Bahadur, S.V. Garimella, Electrical actuation of electrically conducting and insulating droplets using ac and dc voltages, J. Micromech. Microeng. 18 (2008).

[29] J.M. Roux, J.L. Achard, Y. Fouillet, Forces and charges on an undeformable droplet in the DC field of a plate condenser, J. Electrostat. 66 (2008) 283–293.

[30] L. Chen, E. Bonaccurso, Electrowetting — From statics to dynamics, Adv. Colloid Interface Sci. 210 (2014) 2–12.

[31] J.Z. Chen, A.A. Darhuber, S.M. Troian, S. Wagner, Capacitive sensing of droplets for microfluidic devices based on thermocapillary actuation, Lab Chip 4 (2004) 473–480.

[32] J. Kim, M. Kaviany, Electrowetting purged surface condensate in evaporators, Heat Transf. Eng. 31 (2010) 101–107.

[33] R. Dey et al., Controlling shedding characteristics of condensate drops using electrowetting, Appl. Phys. Lett. 113 (2018).

[34] R. Yan et al., Enhanced water capture induced with electrowetting-on-dielectric (EWOD) approach, Appl. Phys. Lett. 113 (2018) 204101.

[35] S. Chavan et al., Heat transfer through a condensate droplet on hydrophobic and nanostructured superhydrophobic surfaces, Langmuir 32 (2016) 7774–7787.

[36] N. Watanabe, M. Aritomi, A. Machida, Time-series characteristics and geometric structures of drop-size distribution density in dropwise condensation, Int. J. Heat Mass Transf. 76 (2014) 467–483.

[37] X. Ma, X. Zhou, Z. Lan, Y. Li, Y. Zhang, Condensation heat transfer enhancement in the presence of non-condensable gas using the interfacial effect of dropwise condensation, Int. J. Heat Mass Transf. 51 (2008) 1728–1737.

[38] F.P. Incropera, D.P. Dewitt, T.L. Bergman, A.S. Lavine, Fundamentals of heat and mass transfer, sixth ed., WILEY, 2006.

[39] V.P. Carey, Liquid-vapor phase-change phenomena: an introduction to the thermophysics of vaporization and condensation processes in heat transfer equipment, Taylor and Francis, 2008.

[40] E.D. Wikramanayake, V. Bahadur, Flared natural gas-based onsite atmospheric water harvesting (AWH) for oilfield operations, Environ. Res. Lett. 11 (2016) 034024.